

# Experimental Realization of Discrete Time Quasicrystals

Guanghui He<sup>1,\*</sup>, Bingtian Ye<sup>2,\*†</sup>, Ruotian Gong<sup>1</sup>, Changyu Yao<sup>1</sup>, Zhongyuan Liu<sup>1</sup>, Kater W. Murch<sup>1,3</sup>,  
Norman Y. Yao<sup>2</sup> and Chong Zu<sup>1,3,4,‡</sup>

<sup>1</sup>Department of Physics, Washington University, St. Louis, Missouri 63130, USA

<sup>2</sup>Department of Physics, Harvard University, Cambridge, Massachusetts 02138, USA

<sup>3</sup>Center for Quantum Leaps, Washington University, St. Louis, Missouri 63130, USA

<sup>4</sup>Institute of Materials Science and Engineering, Washington University,  
St. Louis, Missouri 63130, USA



(Received 10 April 2024; revised 4 December 2024; accepted 21 January 2025; published 12 March 2025)

Floquet (periodically driven) systems can give rise to unique nonequilibrium phases of matter without equilibrium analogs. The most prominent example is the realization of discrete time crystals. An intriguing question emerges: What other novel phases can manifest when the constraint of time periodicity is relaxed? In this study, we explore quantum systems subjected to a quasiperiodic drive. Leveraging a strongly interacting spin ensemble in diamond, we identify the emergence of long-lived discrete time quasicrystals. Unlike conventional time crystals, time quasicrystals exhibit robust subharmonic responses at multiple incommensurate frequencies. Furthermore, we show that the multifrequency nature of the quasiperiodic drive allows for the formation of diverse patterns associated with different discrete time quasicrystalline phases. Our findings demonstrate the existence of nonequilibrium phases in quasi-Floquet settings, significantly broadening the catalog of novel phenomena in driven many-body quantum systems.

DOI: [10.1103/PhysRevX.15.011055](https://doi.org/10.1103/PhysRevX.15.011055)

Subject Areas: Quantum Physics, Quantum Information

## I. INTRODUCTION

Spontaneous symmetry breaking is fundamental in all fields of physical sciences [1]. In the context of many-body physics, the emergence of distinct phases can be viewed through the lens of different types of symmetry breaking [2]. The most prominent example is probably the formation of crystals from breaking the translational symmetry in space. Its cousin in the time domain, the recently discovered discrete time crystal (DTC), breaks the time-translation symmetry [3–42]. For quite a long time, periodicity and long-range order have been believed to be the two intimately correlated characteristics of crystalline phases [33,43,44]. Quasicrystals are an exception: They are ordered but not apparently periodic [45,46]. The hidden periodicity can be thought

of as a higher-dimensional periodic crystal projecting onto a lower-dimensional subspace. A natural question arises as to whether one can make an analogy in the time domain to create time quasicrystalline orders.

To answer this question, one can first draw intuition from the creation of a conventional time crystal. Since the quantum equilibrium state of a time-independent Hamiltonian cannot have time-dependent observables, the construction of a time crystal is possible only in systems with discrete time-translation symmetry, i.e., in a periodically driven (Floquet) system [47–49].

The construction of a DTC relies on the concept of emergent symmetry which does not exist in the native time-dependent Hamiltonian; instead, it is induced by the time-translation symmetry. A characteristic of the DTC phase is that the physical observable exhibits a longer period than the driving field [50]. A prototypical example is the dynamical decoupling sequence with a train of evenly spaced  $\pi$  pulses, where the effective Hamiltonian in the “toggling” frame exhibits a  $\mathbb{Z}_2$  Ising symmetry that is independent of the symmetry of the initial Hamiltonian. The breaking of such emergent symmetry then enables the system to display a subharmonic response. Crucially, as a phase of matter (in contrast to fine-tuned Floquet engineering techniques), the key ingredient is the robustness of the above-mentioned subharmonic response to perturbations.

\*These authors contributed equally to this work.

†Contact author: [bingtian\\_ye@g.harvard.edu](mailto:bingtian_ye@g.harvard.edu)

‡Contact author: [zu@wustl.edu](mailto:zu@wustl.edu)

Published by the American Physical Society under the terms of the [Creative Commons Attribution 4.0 International](https://creativecommons.org/licenses/by/4.0/) license. Further distribution of this work must maintain attribution to the author(s) and the published article's title, journal citation, and DOI.

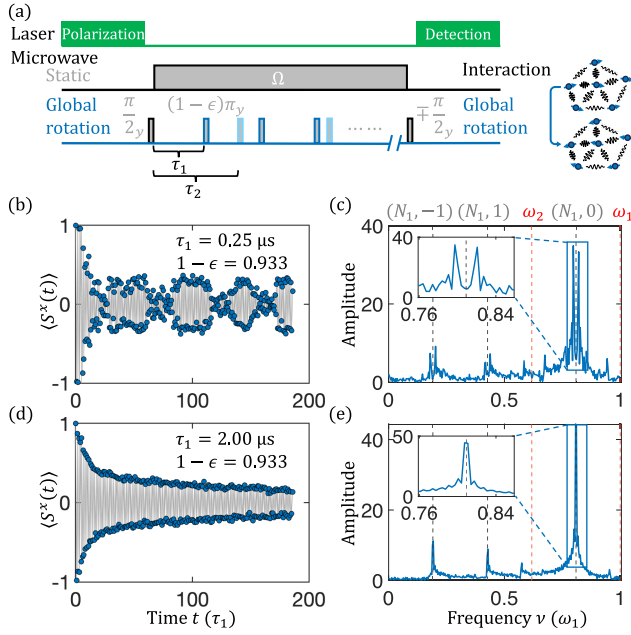


FIG. 1. Experiment to observe  $\mathbb{Z}_2$  time quasicrystalline order. (a) Pulse sequence for the experiment. After laser polarization, a  $\pi/2$  pulse along the  $\hat{y}$  axis initializes the spin ensemble to  $|+x\rangle$ , followed by a time-independent static microwave drive  $\Omega \sum S_i^x$ . The quasiperiodic drives consist of a series of global pulses with rotation angle  $(1-\epsilon)\pi$  applied with incommensurate frequencies  $\omega_1 = 2\pi/\tau_1$  and  $\omega_2 = 2\pi/\tau_2$ . A final  $\mp(\pi/2)$  pulse along the  $\hat{y}$  axis flips the spins back to  $\hat{z}$  basis for measurement. (b)–(e) Representative spin polarization dynamics and the corresponding Fourier spectrum under quasiperiodic drive with  $[\tau_1 = 0.25 \mu\text{s}, 1-\epsilon = 0.933]$  (b),(c) and  $[\tau_1 = 2.00 \mu\text{s}, 1-\epsilon = 0.933]$  (d),(e). Gray dashed lines, labeled by  $(N_1, N_2)$ , indicate the subharmonic response frequencies of DTQC. Red dashed lines mark the quasiperiodic driving frequencies. Insets: enlargement of the subharmonic response at  $(N_1, 0)$ .

To go beyond DTC and create a discrete time quasicrystal (DTQC), a straightforward idea is to replace the periodically applied  $\pi$  pulses with a quasiperiodic manner, where the rigidity of the crystalline order becomes a more complex question. Note that the term “DTQC” has also been used for systems that exhibit a quasiperiodic response arising from periodic drive, where the frequencies of the response, in general, depends on the microscopic parameters of the system [30,51]. In addition, a recent work on “rondeau time crystal” also goes beyond conventional DTC by introducing random but structured driving protocol [42].

In this paper, we investigate the DTQC order using a strongly interacting ensemble of nitrogen-vacancy (NV) centers in diamond. Our results are in threefold. First, we observe the DTQC order manifests as the responses at halves of the linear combinations of two

incommensurate driving frequencies (Fig. 1). Second, with regard to the robustness of the DTQC order, we find that the strong many-body interaction within the spin ensemble provides rigidity against perturbations (Fig. 2). We quantify this rigidity by characterizing the competition between the interaction strength and the magnitude of the perturbation per unit time,  $\epsilon/\tau_1 + \epsilon/\tau_2$ , to map out the phase diagram of DTQC (Fig. 3). Third, we show that the multifrequency nature of the quasiperiodic drives allows one to incorporate multiple symmetries into the effective Hamiltonian and realize more complicated DTQCs. For instance, by leveraging two different crystallographic groups of NV centers, we investigate the  $\mathbb{Z}_2 \times \mathbb{Z}_2$  DTQC phase (Fig. 4).

## II. RESULTS

### A. Observing DTQC order

To experimentally realize DTQC, we refine the aforementioned intuition into a concrete quasi-Floquet Hamiltonian:

$$\mathcal{H}(t) = \sum_{i<j} (J_{i,j} S_i^x S_j^x) + \Omega \sum_i S_i^x + (1-\epsilon) \sum_i S_i^y \left[ \sum_{n_1} \delta(t - n_1 \tau_1) + \sum_{n_2} \delta(t - n_2 \tau_2) \right], \quad (1)$$

where  $\hat{S}$  is the spin operator,  $n_1, n_2 \in \mathbb{Z}$ , and  $|\epsilon| \ll 1$  represents a small perturbation on top of perfect  $\pi$ -pulse rotations. The first two terms correspond to the time-independent component of the many-body spin Hamiltonian, and the last term is the quasiperiodic spin flip performed with frequencies  $\omega_1 = 2\pi/\tau_1$  and  $\omega_2 = 2\pi/\tau_2$ . We choose the ratio  $\varphi = \omega_1/\omega_2 = (\sqrt{5} + 1)/2 \approx 1.618$  as the golden ratio so that the two driving frequencies are the most incommensurate to each other.

To implement the quasi-Floquet Hamiltonian, we choose to work with a diamond sample containing a dense ensemble of NV centers (approximately 4.5 ppm). Each NV center is a spin-1 artificial atom that can be optically initialized and readout. By applying an external magnetic field, we lift the degeneracy of  $|m_s = \pm 1\rangle$  via Zeeman splitting and isolate an effective spin-1/2 system spanned by  $\{|m_s = 0\rangle, |m_s = -1\rangle\}$ . Under a static driving field along the  $\hat{x}$  direction, the Hamiltonian governing the dipolar interacting NV ensemble takes the form

$$\mathcal{H}_0 = - \sum_{i<j} J_{i,j} (S_i^z S_j^z - S_i^x S_j^x - S_i^y S_j^y) + \sum_i h_i S_i^z + \Omega \sum_i S_i^x, \quad (2)$$

where  $J_{i,j} \sim (2\pi) \times 52 \text{ MHz} \cdot \text{nm}^3 / r_{i,j}^3$  with  $r_{i,j}$  the distance between the  $i$ th and  $j$ th spins,  $h_i$  characterizes the on-site random field, and  $\Omega$  is the Rabi frequency of the drive.

A few remarks are in order. First, we set the microwave strength [ $\Omega = (2\pi) \times 8.3 \text{ MHz}$ ] to be much larger than both the average dipolar interaction strength between two nearby NVs [ $\bar{J}_{i,j} \approx (2\pi) \times 0.05 \text{ MHz}$ ] and the magnitude of the on-site random field [ $\bar{h}_i \approx (2\pi) \times 1.7 \text{ MHz}$ ], so that all the terms that do not commute with  $S_i^x$  are significantly suppressed. In this limit, the many-body Hamiltonian in Eq. (2) can be well-approximated by  $\mathcal{H}_0 \approx \sum_{i<j} (J_{i,j} S_i^x S_j^x) + \Omega \sum_i S_i^x$ , corresponding to the first two terms of our quasi-Floquet Hamiltonian [Eq. (1)]. Second, the quasiperiodic driving terms of the Hamiltonian can be realized via series of global microwave pulses along the  $\hat{y}$  axis with rotation angle  $(1 - \epsilon)\pi$  at times  $t = n_1\tau_1$  and  $n_2\tau_2$ . Third, the random positioning of the NV centers can introduce strong disorder to the spin-spin interaction term  $J_{i,j}$ , leading to slow critical thermalization of the spin dynamics as demonstrated in previous works [43,52]. Therefore, although the DTQC order studied in this work does not exhibit an infinitely long lifetime due to the absence of many-body localization, strong disorder still prevents the system from approaching a prethermal state [53] and enables a long-lived DTQC order within the relevant times investigated in experiment.

With all the ingredients in hand, we now turn to the full experimental sequence shown in Fig. 1(a). After the optical pumping, the NV system is initialized to  $|+\rangle = \otimes_i (|0\rangle_i + |-1\rangle_i / \sqrt{2})$  by applying a global  $\pi/2$  pulse around the  $\hat{y}$  axis, followed by the quasiperiodic drives. Let us first consider a simple scenario. In the case of  $\epsilon \approx 0$ , each microwave pulse precisely rotates the spin ensemble halfway around the Bloch sphere at integer times of  $\tau_1$  and  $\tau_2$ , so the sign of the average magnetization along the  $\hat{x}$  axis,  $\langle S^x(t) \rangle$ , will flip at the corresponding times, while the amplitude will remain constant, in principle, but subject to a slow decay due to the combination of pulse imperfections as well as intrinsic spin relaxation ( $T_1$ ) process in the experiment. In the Fourier space, the measured magnetization dynamics manifests a series of “subharmonic” peaks at frequencies [55]:

$$\nu = \left(N_1 + \frac{1}{2}\right)\omega_1 + \left(N_2 + \frac{1}{2}\right)\omega_2, \quad N_1, N_2 \in \mathbb{Z}. \quad (3)$$

One may naively consider such dynamics as the DTQC order. However, the aforementioned picture relies on the fine-tuning of the experimental parameters; i.e., the rotation pulses need to be perfect. In order to

establish a real phase of matter, we have to investigate the rigidity of the “subharmonic” responses against the imperfections of the  $\pi$  rotations.

For a relatively short driving period,  $\tau_1 = 0.25 \mu\text{s}$  and  $\tau_2 = 0.404 \mu\text{s}$ , in the presence of pulse imperfections,  $1 - \epsilon \approx 0.933$ , we observe a clear beating in the measured spin dynamics [Fig. 1(b)]. In the corresponding Fourier spectrum, we observe that the three dominant subharmonic responses marked with  $(N_1, N_2)$  at  $(N_1, 0)$ ,  $(N_1, -1)$ , and  $(N_1, 1)$  each split into two peaks [Fig. 1(c)], suggesting the breakdown of the DTQC order. We note that, in the presence of quasiperiodic rotations, there does not exist a stroboscopic time that one can measure the spin dynamics. As a result, we can probe the spin dynamics with a much faster sampling frequency  $\omega_s = 10\omega_1$  or shorter time period  $\tau_1/10$ . However, we also verify that, when sampling at the quasiperiodic time,  $\tau = n_1\tau_1$  and  $n_2\tau_2$ , one can still faithfully obtain the spin dynamics and the associated Fourier spectrum (see Appendix B). This also distinguishes our dynamical features from the recently introduced time rondeau crystal that exhibits a repeated dynamical pattern only at stroboscopic times [42].

Surprisingly, for a long driving period ( $\tau_1 = 2 \mu\text{s}$ , and  $\tau_2 = 3.236 \mu\text{s}$ ) with the same magnitude of the pulse imperfections, the measured dynamics remains ordered up to time  $t \sim 200\tau_1$  [Fig. 1(d)]. The robustness is also evident in the frequency domain—the three dominant “subharmonic” peaks do not split. The distinct dynamical behaviors with different driving periods suggest that the many-body interaction plays a crucial role in stabilizing the DTQC phase. Intuitively, the coupling terms in the Hamiltonian,  $J_{i,j} S_i^x S_j^x$ , provide an energy barrier that prevents the uncorrelated flips of each individual spin caused by the local perturbations, i.e., the imperfect pulse rotation in experiment. This picture becomes clearer when we go into the “toggling frame,” where the spin polarization along the  $\hat{x}$  axis effectively alternates every time we apply the  $\pi_y$  pulse. In this frame, the imperfection rate per unit time,  $\epsilon/\tau_1 + \epsilon/\tau_2$ , of the  $y$  rotation is suppressed by the strong effective interaction  $J_{i,j}$ . We remark that this type of interaction is inherently protected by the emergent  $\mathbb{Z}_2$  symmetry (along  $\hat{x}$ ), which has been shown to be a direct consequence of time periodicity and recently been generalized to quasiperiodicity [45].

Such intuition immediately suggests that, given a driving period  $\tau_1$ , the DTQC behavior should be rigid against imperfections up to certain magnitudes. This is indeed borne out by our data. At  $\tau_1 = 1 \mu\text{s}$ , when  $\epsilon \in [-0.07, 0.05]$ , all three “subharmonic” responses remain rigid [Fig. 2(a)]. When the imperfection goes beyond this regime, all three peaks split, indicating the breakdown of DTQC order.

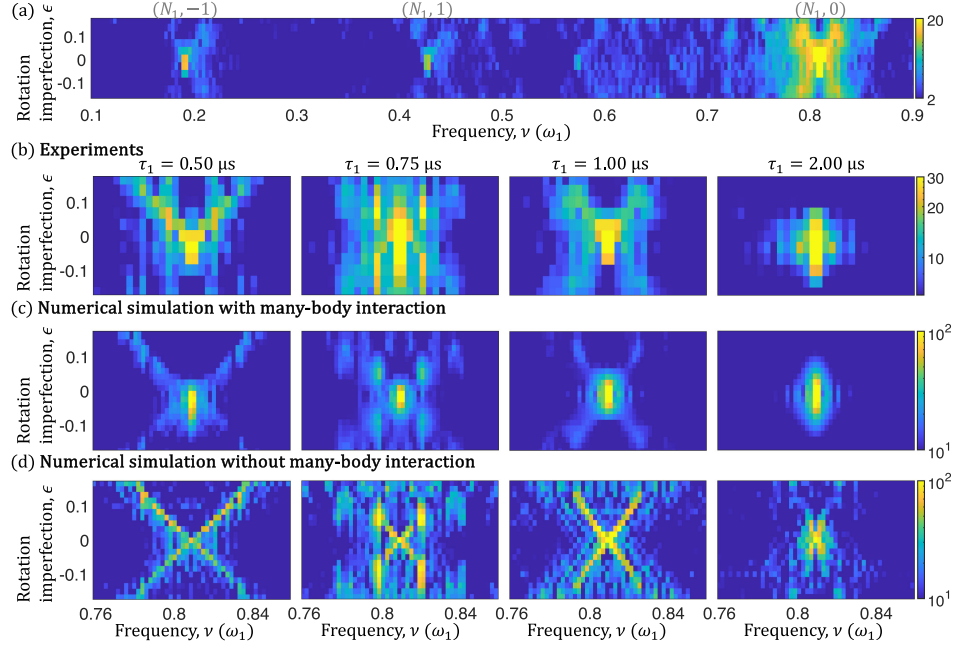


FIG. 2. Rigidity of time quasicrystals. (a) Fourier spectrum of DTQC at  $\tau_1 = 1.00 \mu\text{s}$  with varying rotation imperfections. All three subharmonic responses remain robust when  $\epsilon \in [-0.07, 0.05]$  and split beyond this regime. The color bar indicates amplitude of the Fourier transform. (b)–(d) A comparison between experimental data and numerical simulation [enlarging the response at  $(N_1, 0)$ ]. We observe quantitative agreement between experiments (b) and many-body simulations using 16 disordered spins (c). The numerical simulation without many-body interaction (d) indicates that any small rotation imperfection induces splitting of the subharmonic responses which does not agree with our experimental observations.

## B. Rigidity of DTQC order

To further corroborate that the rigidity of DTQC order originates from the many-body interaction between spins,  $J_{i,j}S_i^x S_j^x$ , we compare our experimental data to the numerical simulations with and without the interaction using 16 randomly positioned NV spins (see Appendix D). Let us focus on the most prominent subharmonic peak,  $(N_1, 0)$ . In the absence of many-body interactions, any small  $\epsilon$  will lead to the splitting of the peaks across all driving periods  $\tau_1$  [Fig. 2(d)], in sharp contrast to the experimental observations [Fig. 2(b)]. When adding the interactions into the system Hamiltonian, the numerics can reproduce the robustness of DTQC order observed in experiment [Fig. 2(c)]. We further corroborate the role of interaction by observing the breakdown of DTQC order in a diamond sample with much lower NV density, resulting in substantially reduced interaction strength (see Appendix C).

Crucially, when the imperfection rate per unit time decreases, we observe that the DTQC order becomes more robust. To quantify this, we first define a crystalline fraction

$$f(\epsilon) = \frac{|S(\nu_0)|}{\sum_{\nu_0-\delta}^{\nu_0+\delta} |S(\nu)|}, \quad (4)$$

where  $\nu_0$  denotes the frequency of the subharmonic peak labeled by  $(N_1, N_2 = 0)$  and  $\delta = 0.1\omega_1$  so that it does not

overlap with the other peaks. As expected, with a long driving period ( $\tau_1 = 2 \mu\text{s}$ ), the crystalline fraction vanishes at a significantly larger imperfection value compared to the short driving period case ( $\tau_1 = 0.5 \mu\text{s}$ ) [Fig. 3(a)].

To map out the phase boundary for the DTQC order, we determine the critical imperfection  $\epsilon_c(\tau_1)$  such that the crystalline fraction meets the threshold  $f(\epsilon_c) = 0.05$ . Figure 3(b) shows the extracted phase diagram of the DTQC order. We apply the same strategy to the other two subharmonic harmonics responses, as well as the numerical simulations. Interestingly, the phase boundaries determined by the distinct subharmonic responses are consistent with each other and also agree well with the numerics. The coexistence of the subharmonic peaks marks a unique feature of the DTQC phase.

A few points need to be addressed. First, in both experiment and simulation, the phase boundary saturates around  $\tau_1 \gtrsim 2 \mu\text{s}$ , suggesting that the rigidity of DTQC cannot be further enhanced by simply extending the driving period  $\tau_1$ . Stabilizing DTQC order until arbitrarily late time requires many-body localization (MBL) [56–61]. However, MBL is believed to not exist in 3D disordered dipolar spin ensembles. An alternative solution is Floquet prethermalization [40, 54, 62–64]. While such a phenomenon, in general, can be applied to our system, it requires the evolution to start from a low-temperature initial state, which is not satisfied in 3D dipolar spin



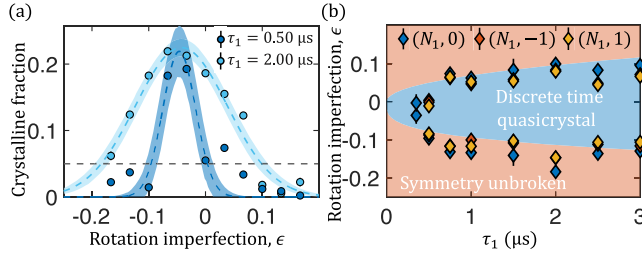


FIG. 3. Phase diagram. (a) Crystalline fraction  $f(\nu)$  as a function of rotation imperfection for  $(N_1, 0)$  subharmonic response. Dashed blue curves are Gaussian fits to the data, and the shaded area indicates fitting uncertainties accounting for one standard deviation. Phase boundary is phenomenologically defined as 5% of the crystalline fraction, marked by the horizontal gray dashed line. The phase boundary extends with a longer driving period. (b) The phase diagram extracted using three distinct subharmonic responses  $(N_1, 0)$  [blue],  $(N_1, -1)$  [red], and  $(N_1, 1)$  [yellow] are consistent with each other. The boundaries extend with increasing  $\tau_1$  and saturate around 2  $\mu\text{s}$ . Background colors mark the phase boundary obtained from the many-body numerical simulation using  $N = 16$  disordered spins.

ensemble. As a result, the DTQC order demonstrated in this work still suffers from thermalization; nevertheless, it is suppressed by the presence of strong positional disorder of the NV ensemble (see Appendix H), giving rise to the long lifetime of the observed DTQC behavior [43,52].

Second, at a certain driving period and imperfection range (e.g., at  $\tau_1 = 0.75 \mu\text{s}$  and  $\epsilon \in [0.05, 0.12]$ ), we observe that the splitting of the subharmonic response exhibits a few segmented plateaus [Figs. 2(b)–2(d)]. Such a feature is present even in the noninteracting scenarios, and we attribute it to the complex interplay between the strong locking field  $\Omega$  and the quasiperiodic rotation pulses. Third, one may naively think that the crystalline fraction  $f(\epsilon)$  should be symmetric around  $\epsilon = 0$ . However, in both experiment and simulations, we find that the maximum value of  $f(\epsilon)$  is slightly shifted to  $\epsilon \approx -0.04$  (Fig. 3). This is due to the presence of on-site random field  $\sum_i h_i S_i^z$ , which leads to a faster spin rotation with an effective Rabi frequency,  $\Omega^{\text{eff}} = \sqrt{\Omega^2 + \bar{h}_i^2}$ .

### C. $\mathbb{Z}_2 \times \mathbb{Z}_2$ DTQC

The aforementioned DTQC order is featured by the measured total polarization oscillating between two distinct values at subharmonic frequencies, reflecting the underlying emergent  $\mathbb{Z}_2$  Ising symmetry along  $\hat{x}$ . Here, utilizing two crystallographic groups of NV centers, we turn to constructing a more complex DTQC with  $\mathbb{Z}_2 \times \mathbb{Z}_2$  symmetry. In particular, the interaction Hamiltonian including two groups of NV centers modifies Eq. (1) to

$$\begin{aligned} \mathcal{H}(t) = & \sum_{\substack{i,j \in A \\ \text{or } i,j \in B}} (J_{i,j} S_i^x S_j^x) + \sum_{\substack{i \in A \\ \text{and } j \in B}} (J'_{i,j} S_i^z S_j^z) + \Omega \sum_{i \in A \text{ and } B} S_i^x \\ & + (1 - \epsilon) \sum_{i \in A \text{ and } B} S_i^y \left[ \sum_{n_1} \delta(t - n_1 \tau_1) \right] \\ & + (1 - \epsilon) \sum_{i \in A} S_i^y \left[ \sum_{n_2} \delta(t - n_2 \tau_2) \right]. \end{aligned} \quad (5)$$

Here,  $A$  and  $B$  refer to two different groups of NV centers, between which the intergroup interaction is governed by the Ising term. We choose the static Rabi driving strength  $\Omega$  to be the same for groups  $A$  and  $B$ , so that the intergroup interaction becomes resonant (see Appendix G). We perform global rotations along the  $\hat{y}$  axis for both groups at time  $n_1 \tau_1$  and a rotation only for group  $A$  at time  $n_2 \tau_2$ . The underlying emergent symmetry of the system is expanded to  $\mathbb{Z}_2 \times \mathbb{Z}_2$ , where the two  $\mathbb{Z}_2$  symmetries correspond to spin rotations for both groups and a single group  $A$ , respectively [Fig. 4(a)].

Next, we investigate the subharmonic response of the resulting  $\mathbb{Z}_2 \times \mathbb{Z}_2$  DTQC by probing the total polarization dynamics of both groups. The representative spin dynamics with  $\tau_1 = 1 \mu\text{s}$  and  $\epsilon = 0$  is shown in Fig. 4(b). In sharp contrast to the  $\mathbb{Z}_2$  scenario, we observe the spin dynamics oscillates among three discrete values. Since the rotations for two NV groups are performed at incommensurate times, there is an additional zero polarization when two groups of NV centers are antialigned. Although the order parameter appears to be zero, the system still remains ordered during these specific time segments rather than reaching to an equilibrium state. The corresponding Fourier spectrum also reflects the same physics [Fig. 4(c)]: There exist four dominant subharmonic peaks at  $\{[(N_1 + \frac{1}{2})\omega_1 + \frac{1}{2}\omega_2], [(N_1 + \frac{1}{2})\omega_1 - \frac{1}{2}\omega_2], [(N_1 + \frac{1}{2})\omega_1 + \frac{3}{2}\omega_2], \frac{1}{2}N_1\omega_1\}$ .

To explore the effect of intergroup interaction on the stability of  $\mathbb{Z}_2 \times \mathbb{Z}_2$  DTQC, we analyze the corresponding DTQC phase boundary with rotation imperfections. Specifically, we compare the measured crystalline fraction with and without the interaction between two NV groups. In experiments, we toggle the intergroup interaction by addressing the two NV groups with either the same Rabi frequency  $\Omega$  (referred to as “with interaction”) or with detuned Rabi frequencies (referred to as “without interaction”). The mismatch in frequency reduces the Ising term to zero, effectively decoupling the two groups. As shown in Fig. 4(d), with interactions, the crystalline fraction at subharmonic frequency  $\frac{1}{2}\omega_1$  vanishes at relatively larger imperfection values compared to the noninteracting case, suggesting that the DTQC phase could be more robust in the presence of intergroup interaction. Intuitively, this additional robustness may reflect the fact that the two groups oscillate collectively due to the intergroup interaction, which provides a larger

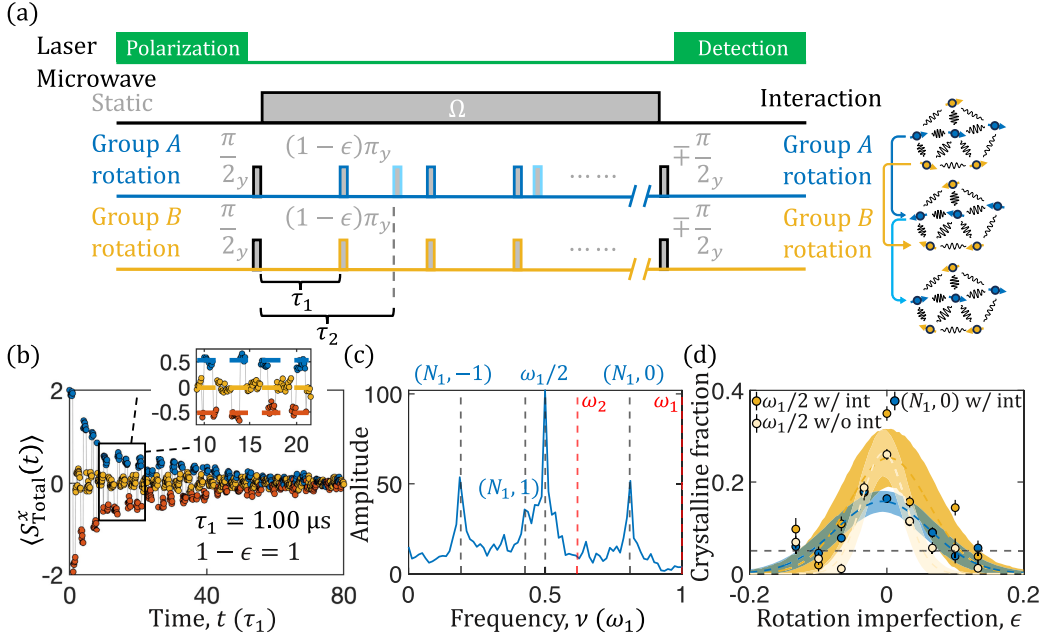


FIG. 4. Observing  $\mathbb{Z}_2 \times \mathbb{Z}_2$  time quasicrystalline order. (a) Experimental pulse sequence. Global rotations are applied at times  $t = n_1\tau_1$  for both NV groups and at times  $t = n_2\tau_2$  only for group B. The total spin polarization for both NV groups is measured at the end. (b) Representative polarization dynamics with  $\tau_1 = 1 \mu\text{s}$  and  $\epsilon = 0$ . The sampling rate is set to be  $10\omega_1$ . Markers change colors as a rotation pulse is applied. Inset: enlargement of the polarization dynamics oscillating among three discrete values. (c) Fourier spectrum of the total polarization dynamics. Four dominant subharmonic responses at frequencies  $\{[(N_1 + \frac{1}{2})\omega_1 + \frac{1}{2}\omega_2], [(N_1 + \frac{1}{2})\omega_1 - \frac{1}{2}\omega_2], [(N_1 + \frac{1}{2})\omega_1 + \frac{3}{2}\omega_2], \frac{1}{2}N_1\omega_1\}$  are marked with dashed lines. Red dashed lines are the quasiperiodic driving frequencies. (d) The extracted crystalline fraction at  $\frac{1}{2}N_1\omega_1$  with (dark yellow) and without (light yellow) intergroup interaction for  $\tau_1 = 1.00 \mu\text{s}$ . We also examine the crystalline fraction at  $(N_1, 0)$  with intergroup interaction (blue), whose width is consistent with the  $\frac{1}{2}\omega_1$  response. Dashed lines are Gaussian fits, and the shaded area indicates fitting uncertainties accounting for one standard deviation.

energy barrier that prevents the uncorrelated flips of the spins in each individual NV group.

### III. CONCLUSION AND OUTLOOK

Our results have presented the first experimental evidence that long-lived robust DTQC can be realized in quasiperiodically driven many-body quantum systems. Such DTQC order is fundamentally distinct with those achieved using conventional Floquet Hamiltonian, greatly expanding the landscape of possible nonequilibrium phases of matter. In particular, DTQC bridges the gap between spatial and temporal quasicrystals, offering a new paradigm for studying intricate symmetry-breaking phenomena in time.

Looking forward, our work opens up a few intriguing directions. For instance, the existence of long-lived DTQC in our 3D dipolar interacting NV ensemble relies on slow critical thermalization. However, in this framework, the lifetime of DTQC cannot be extended to arbitrarily late times. To overcome this, one can construct many-body localized or prethermal DTQC using synthetic quantum platforms such as cold atoms and superconducting

qubits [33,44,63] as well as spin defects in lower dimensions [40,61,65–67]. Additionally, exploring DTQC on such platforms could pave the way for practical applications, such as multifrequency time references for precision measurements and signal processing. These features highlight the potential of DTQCs as versatile tools in advancing quantum technologies. Moreover, it would be interesting to explore, both theoretically and experimentally, the existence of other novel nonequilibrium phases of matter beyond DTQC in driven many-body quantum systems.

### ACKNOWLEDGMENTS

B. Ye acknowledges support from the NSF via the Center for Ultracold Atoms and the STAQ program. N. Y. Y acknowledges support from the U.S. Department of Energy via the QuantISED 2.0 program (Geoflow), the Army Research Office (Grant No. W911NF-24-1-0079), and a Simons Investigator award.

### DATA AVAILABILITY

The data that support the findings of this article are openly available [68]; embargo periods may apply.

## APPENDIX A: EXPERIMENTAL SETUP

We characterize the dynamics of NV centers using a home-built confocal laser microscope. A 532 nm laser (Millennia eV High Power CW DPSS laser) is used for both NV spin initialization and detection. The laser is shuttered by an acousto-optic modulator (AOM, G&H AOMO 3110-120) in a double-pass configuration to achieve  $>10^5:1$  on/off ratio. An objective lens (Nikon Plan Fluor 100 $\times$ ) focuses the laser beam to a diffraction-limited spot with diameter approximately 0.5  $\mu\text{m}$  and collects the NV fluorescence. The fluorescence is then separated from the laser beam by a dichroic mirror and filtered through a long-pass filter before being detected by an avalanche photodiode (Thorlabs). The signal is processed by a data acquisition device (National Instruments USB-6343). The objective lens is mounted on a piezo objective scanner (Physik Instrumente PD72Z1x PIFO), which controls the position of the objective and scans the laser beam vertically. The lateral scanning is performed by an X-Y galvanometer (Thorlabs GVS212).

The NV centers are created randomly in the sample, so there exist four different crystalline orientations of the spin defects. To isolate one group of NV centers, we position a permanent magnet near the diamond to create an external magnetic field  $B \sim 324$  G along one of the NV axes. Under this magnetic field, the  $|m_s = \pm 1\rangle$  sublevels of the aligned NV group are separated due to Zeeman effect and exhibit a splitting  $2\gamma_e B$ , where  $\gamma_e = (2\pi) \times 2.8$  MHz/G is the gyro-magnetic ratio of the NV electronic spin. A resonant microwave drive with frequency  $(2\pi) \times 1.963$  GHz is applied to address the NV transition between  $|m_s = 0\rangle \Leftrightarrow |m_s = -1\rangle$  sublevels and isolate an effective two-level system. We note that at this magnetic field, after a few microseconds of laser pumping, the associated spin-1  $^{14}\text{N}$  nuclear spin of the NV center is highly polarized to  $|m_I = +1\rangle$  via the excited state level anticrossing [69–71].

The microwave driving field is generated by mixing the output from microwave sources (Stanford Research SG384 and SG386) and arbitrary wave generators (AWG, Chase Scientific Wavepond DAX22000). Specifically, a high-frequency signal at  $(2\pi) \times 1.838$  GHz from the microwave source is combined with a  $(2\pi) \times 0.125$  GHz signal from the AWG using a built-in in-phase and quadrature modulator,

so that the sum frequency at  $(2\pi) \times 1.963$  GHz is resonant with the NV  $|m_s = 0\rangle \Leftrightarrow |m_s = -1\rangle$  transition. By modulating the amplitude, duration, and phase of the AWG output, we can control the strength, rotation angle, and axis of the microwave pulses. To realize DTQC, we perform spin rotation at quasiperiodic times  $n_1\tau_1$  and  $n_2\tau_2$ , where  $\varphi = \tau_2/\tau_1 = (\sqrt{5} + 1)/2 \approx 1.61803\dots$ . Note that the driving periods  $\tau_1$  and  $\tau_2$  are on the order of microseconds, while the temporal resolution of the AWG has a limit of 0.5 ns. As a result, we specify  $\varphi$  to be accurate to three decimal places, 1.618. The microwave signal is then amplified by a high-power amplifier (Mini-Circuits ZHL-15W-422-S+) and delivered to the diamond sample through a coplanar wave guide. The microwave is shuttered by a switch (Minicircuits ZASWA-2-50DRA+) to prevent any potential leakage. All equipment are gated through a programmable multichannel pulse generator (SpinCore PulseBlasterESR-PRO 500) with 2 ns temporal resolution.

## APPENDIX B: SAMPLING SCHEME FOR PROBING SPIN DYNAMICS

Because of the presence of quasiperiodic rotations in the microwave pulse sequence, there is no stroboscopic time to probe the spin polarization. There are two alternative sampling schemes. One is to measure the spin dynamics at a much faster frequency than the rotation frequency, such that one can capture the micromotion between rotation pulses. In practice, we choose the sampling frequency to be  $\omega_s = 10\omega_1$ , and the probed spin dynamics is shown in Fig. 5(a) in yellow. A second possible approach is to probe the average polarization after each rotation pulse [blue in Fig. 5(a)] or sampling at the quasiperiodic time. As a consequence, the acquired data points are not evenly spaced in time space, and, thus, one needs to perform nonuniform Fourier transform to extract the subharmonic response frequencies.

Here, we verify that by sampling at the quasiperiodic time,  $t = n_1\tau_1$  and  $t = n_2\tau_2$ , the measured spin dynamics and the corresponding Fourier spectrum agree well with their dense sampling counterparts. Shown in Fig. 5(a), the measured spin dynamics by sampling at discrete times overlaps with the dense sampling one. The corresponding Fourier spectra also faithfully provide the subharmonic response frequencies. In

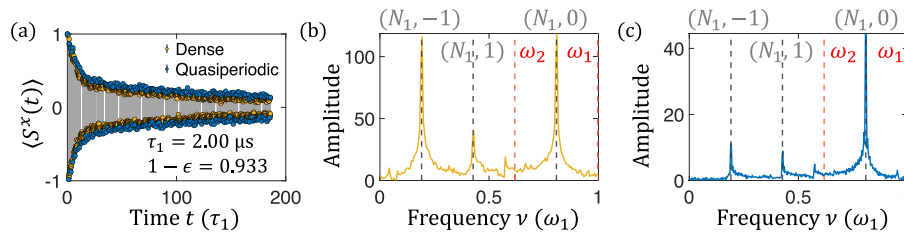


FIG. 5. A comparison between dense and quasiperiodic sampling schemes. (a) Representative spin dynamics with  $\tau_1 = 2.00$   $\mu\text{s}$  and  $1 - \epsilon = 0.933$ , with dense (yellow) and quasiperiodic (blue) sampling schemes. (b) Extracted Fourier spectrum using the dense sampling scheme. (c) Extracted Fourier spectrum using the quasiperiodic sampling scheme. The frequencies of the subharmonic peaks using two methods agree with each other.



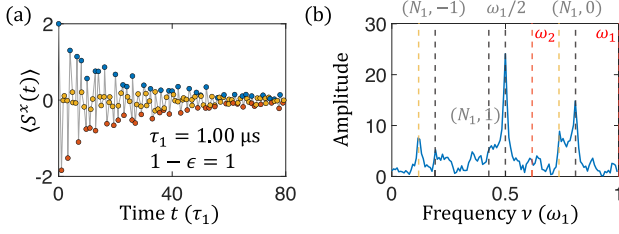


FIG. 6. Sampling  $\mathbb{Z}_2 \times \mathbb{Z}_2$  DTQC with incommensurate frequencies. (a) Typical spin dynamics with  $\tau_1 = 1.00 \mu\text{s}$  and  $1 - \epsilon = 1$ , when sampling at the quasiperiodic time  $t = n_1 \tau_1$  and  $t = n_2 \tau_2$ . (b) The corresponding Fourier transform. Gray dashed lines specify subharmonic frequencies of DTQC, and red dashed lines mark the quasiperiodic driving frequencies. Yellow dashed lines indicate the spurious peaks induced by the discrete sampling scheme.

Figs. 1–3 in the main text, we probe the spin dynamics with the quasiperiodic sampling scheme.

However, for  $\mathbb{Z}_2 \times \mathbb{Z}_2$  DTQC, we find that when probing the spin dynamics with quasi-Floquet frequencies, the extracted Fourier spectrum exhibits multiple spurious peaks. Figure 6 shows the measured spin dynamics in time and frequency space with  $\tau_1 = 1.00 \mu\text{s}$  and  $1 - \epsilon = 1$ . Except from the expected four subharmonic response frequencies, there exist additional peaks related to the discrete sampling scheme (yellow dashed line). To accurately reflect the essence of  $\mathbb{Z}_2 \times \mathbb{Z}_2$  DTQC, we utilize the dense sampling scheme in Figs. 4(b) and 4(c) in the main text. Nevertheless, when we compare the crystalline fraction at subharmonic frequency  $\frac{1}{2}\omega_1$  in Fig. 4(d) in the main text, we adopt the quasiperiodic sampling scheme, since the spurious peaks do not affect the position of the subharmonic peaks.

### APPENDIX C: THE ROLE OF INTERACTION IN PROTECTING DTQC ORDER

To further corroborate our claim about the critical role of interaction in protecting DTQC order, we conduct additional experiments using a diamond sample with a significantly lower NV density (approximately 0.01 ppm),

which is approximately 100 times more dilute than the sample used in the main text. This reduction in NV density effectively reduces the dipolar interaction strength, allowing us to investigate the interaction-driven stabilization of the DTQC order more directly.

Figure 7 presents a comparison between the experimental results obtained from the dense NV sample (as used in the main text) and the dilute NV sample. Shown in Figs. 7(a) and 7(b), the spin polarization dynamics are shown for both samples at  $\tau_1 = 1.00 \mu\text{s}$  and a rotation imperfection of  $1 - \epsilon = 0.967$ . For the dense NV sample (dark blue), the spin dynamics remain ordered up to  $t \sim 200\tau_1$ . In contrast, the dilute NV sample (light blue) exhibits a clear beating pattern in the time trace, indicating a breakdown of the DTQC order. Moreover, Fig. 7(c) compares the measured crystalline fraction for interaction times  $\tau_1 = 0.75 \mu\text{s}$ . The results show that the crystalline fraction for the dilute NV sample is consistently lower than that of the dense NV sample, suggesting a smaller DTQC regime.

These experimental observations provide direct evidence that the interaction strength plays a crucial role in stabilizing the DTQC order, thereby enhancing the impact of our work, as it validates the interaction-driven stabilization mechanism proposed in the simulations.

### APPENDIX D: NUMERICAL SIMULATION

The numerical simulation is implemented using Krylov subspace eigensolving via Dynamite [72]. The dipolar interaction Hamiltonian is built up using Eq. (2) in the main text. The bath spin density is set to be  $\rho_{1/4} = 1.125 \text{ ppm}$ . The subscript denotes  $\frac{1}{4}$  of the total NV density in our sample, since we perform experiments on only one of the four NV groups. We generate a Gaussian distributed on-site random field  $h_z S_i^z$ , with a standard deviation of 1.7 MHz, which agrees with the experiments. For each simulation, we average 50 realizations of positional disorder and random field.

To mitigate the finite-size effects, we specifically focus on analyzing the polarization dynamics of the center spin surrounded by 15 randomly positioned spins. Additionally,

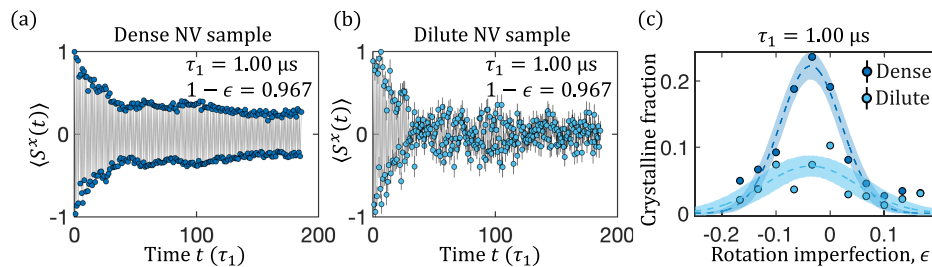


FIG. 7. Comparison of DTQC dynamics in dense and dilute NV samples. (a) Time evolution of spin polarization at  $\tau_1 = 1.00 \mu\text{s}$  and  $1 - \epsilon = 0.967$  for dense (dark blue) and dilute (light blue) NV samples. The dense sample exhibits DTQC order up to  $t \approx 200\tau_1$ , while the dilute sample shows a beating pattern, marking a breakdown of DTQC order. (b) Crystalline fraction measurements at interaction times  $\tau_1 = 0.75 \mu\text{s}$  and  $\tau_1 = 1.00 \mu\text{s}$  as a function of rotation imperfection  $\epsilon$ . The dilute sample displays a lower crystalline fraction, indicating a diminished DTQC phase under reduced interaction strength compared to the dense sample.



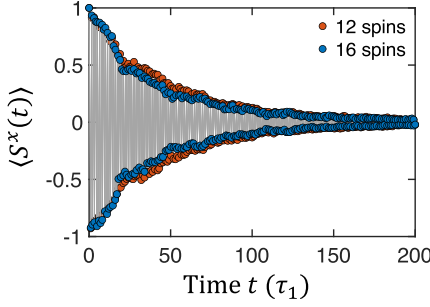


FIG. 8. Comparison of dynamics of different system sizes. Simulated spin dynamics for systems with 16 spins (blue) and 12 spins (red). The simulated spin dynamics remain consistent across system sizes, indicating the system stays robust to finite-size effects. Data are presented for  $\tau_1 = 1.00 \mu\text{s}$  and  $1 - \epsilon = 0.950$ .

we average the dynamics over multiple realizations with varying bath NV geometries to better mimic the experimental configurations and ensure the robustness of our results. These approaches effectively reduce the limitations of a finite spin ensemble in our numerical simulations.

To verify that a system size of 16 spins is sufficient to capture the dynamics in experiment, we perform additional simulations with a smaller system size of  $N = 12$  spins. As shown in Fig. 8, we compare the dynamics of the center spin with  $\tau_1 = 1.00 \mu\text{s}$  and  $1 - \epsilon = 0.950$ , for systems with 12 spins (red) and 16 spins (blue). We find that the simulated dynamics has only a small discrepancy with different system size, indicating that  $N = 16$  spins is more or less enough to capture the dynamics of the system.

We attribute the convergence of the simulated dynamics at small system size to the positional disorder of the NV ensemble. In the presence of strong disorder, the dynamics of the center NV is significantly more influenced by local environment, and the finite-size effect is less important compared to the case with spins on a lattice.

### APPENDIX E: OPTICALLY DETECTED MAGNETIC RESONANCE SPECTRUM

To create DTQC with  $\mathbb{Z}_2 \times \mathbb{Z}_2$  symmetry, we need to address two NV groups individually with distinct microwave frequencies. We achieve this by misaligning the external magnetic field so that it is not parallel to any NV axis. This geometry allows us to isolate two NV groups while separating them from other groups. Additionally, we carefully select the magnetic field orientation to minimize the effects of transverse magnetic coupling for both groups.

Figure 9 shows six peaks in the optically detected magnetic resonance (ODMR) spectrum, corresponding to the transition frequencies of the NV centers. In our experiments, we designate the NV 2  $|m_s = 0\rangle \Leftrightarrow |m_s = +1\rangle$  transition as group A and the NV 1  $|m_s = 0\rangle \Leftrightarrow |m_s = -1\rangle$  transition as group B.

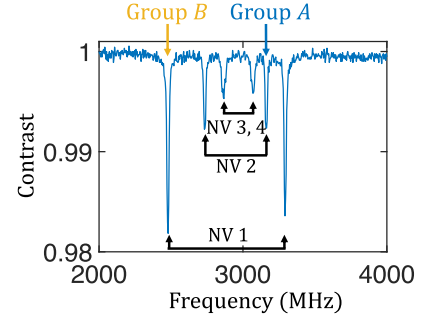


FIG. 9. Optically detected magnetic resonance spectrum of the sample. By misaligning the external magnetic field, the measured ODMR spectrum displays six peaks, indicating distinct NV crystallographic groups.

### APPENDIX F: PULSE SEQUENCE FOR THE $\mathbb{Z}_2 \times \mathbb{Z}_2$ DTQC

In Fig. 4(a) in the main text, we display the experimental pulse sequence for observation of the  $\mathbb{Z}_2 \times \mathbb{Z}_2$  DTQC. However, in real experiments, we need to take finite rotation pulse duration into consideration. Specifically, at time  $n_2\tau_2$ , we apply two additional pulses on group B,  $\{[(1 - \epsilon)\pi/2]_{\hat{x}} - [(1 - \epsilon)\pi/2]_{-\hat{x}}\}$ . The two adjacent pulses are along the exact opposite axis, so that the effects of the two cancel. Meanwhile, the total time duration of the two pulses matches that of the applied rotation pulse on group A, which compensates the time lapse that would otherwise be a redundant  $(1 - \epsilon)\pi_{\hat{x}}$  pulse for group B (Fig. 10).

### APPENDIX G: INTERGROUP INTERACTION BETWEEN TWO NV GROUPS

In the main text, we utilize two crystallographic groups of NV to realize a more complex DTQC with  $\mathbb{Z}_2 \times \mathbb{Z}_2$  symmetry and investigate the effect of intergroup interaction on the robustness of the phase boundary. Here, we verify the existence of the interaction between two groups.

Figure 11 displays the spin-locking contrast reduction, induced by the intergroup interaction. First, we apply

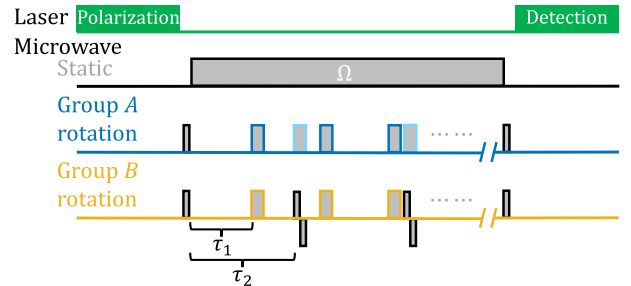


FIG. 10. Pulse sequence for the  $\mathbb{Z}_2 \times \mathbb{Z}_2$  DTQC. A detailed microwave pulse sequence for realizing  $\mathbb{Z}_2 \times \mathbb{Z}_2$  DTQC. On top of the sequence shown in the main text, two adjacent pulses  $\{[(1 - \epsilon)\pi/2]_{\hat{x}}[(1 - \epsilon)\pi/2]_{-\hat{x}}\}$  are applied for group B, in order to compensate the time lapse induced by the finite pulse effect.

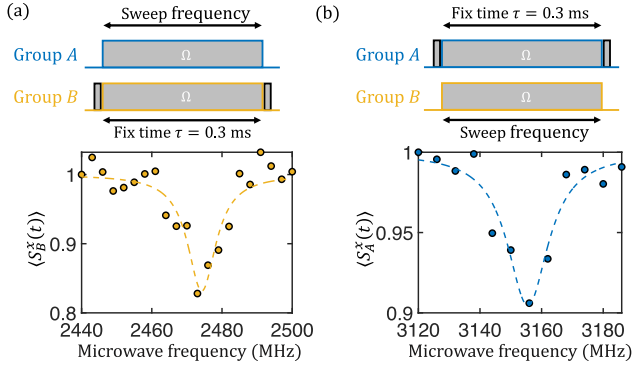


FIG. 11. Demonstration of interaction between groups. (a) A spin-locking sequence with fixed time  $\tau = 0.3$  ms is applied on group  $B$  while sweeping the microwave frequency of a static drive on group  $A$ . The spin polarization of group  $B$  is measured. The polarization exhibits a resonance when the microwave frequency matches that of the group  $A$  transition frequency, due to the fact that the intergroup interaction enhances the dephasing process of group  $B$ . (b) Applying spin-locking drive on group  $A$  and sweeping the static microwave frequency on group  $B$ . A dip is observed when the microwave frequency is in resonance with the transition frequency of group  $B$ .

a spin-locking sequence on group  $B$ , with a fixed duration  $\tau = 0.3$  ms and microwave strength  $\Omega = (2\pi) \times 8.33$  MHz. Then, we apply a static microwave drive on group  $A$  with the same strength  $\Omega$  while sweeping the microwave

frequency. The remaining polarization of group  $B$  is measured. Figure 11(a) shows the spin-locking amplitude as a function of the microwave frequency. A clear resonance is observed when the microwave frequency matches  $|m_s = 0\rangle \Leftrightarrow |m_s = -1\rangle$  transition frequency of group  $A$ , indicating a solid coupling between two groups. We further corroborate this result by performing spin locking on group  $A$  while sweeping static microwave frequency on group  $B$ . Figure 11(b) indicates that the polarization shows a dip when the microwave frequency is in resonance with the  $|m_s = 0\rangle \Leftrightarrow |m_s = +1\rangle$  transition frequency of group  $B$ .

## APPENDIX H: THE ROLE OF POSITIONAL DISORDER IN PROTECTING DTQC ORDER

In our experimental platform, true MBL is not achievable due to the system's high dimensionality (3D) and long-range dipolar interactions. However, the strong disorder in  $J_{i,j}$  still significantly slows down thermalization, a phenomenon referred to as critical thermalization [52]. The underlying intuition is analogous to MBL time crystals [44]. To demonstrate the role of positional disorder in mitigating thermalization, we perform extensive numerical simulations contrasting the dynamics of the system with disordered  $J_{i,j}$ , with simulations of the system on a regular lattice, where

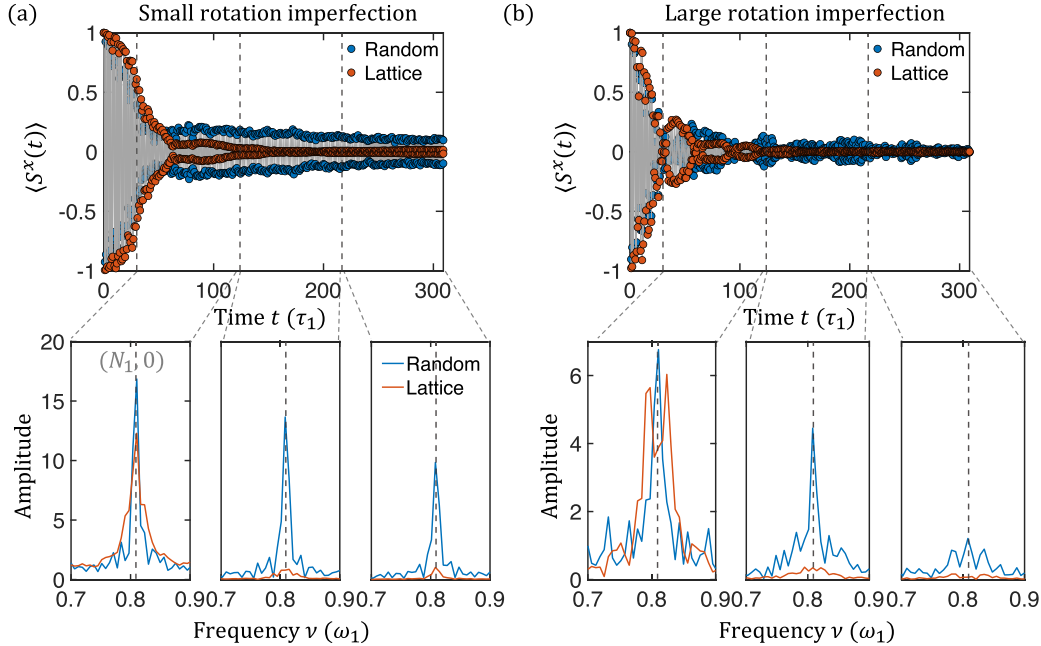


FIG. 12. Disorder-induced stabilization of DTQC dynamics in random and lattice NV configurations. (a) Under small rotation imperfections, the spin polarization  $\langle S^x(t) \rangle$  of randomly distributed NV centers (blue) exhibits robust subharmonic oscillations with a slow decay in amplitude. In contrast, NV centers arranged on a regular lattice (red) show reduced oscillation amplitudes and faster decay, indicating the breakdown of DTQC order. (b) With large rotation imperfections, the subharmonic response for NV centers on a lattice splits into two distinct peaks, while randomly distributed NV centers remain a stable DTQC response, highlighting the key role of positional disorder in stabilizing the DTQC phase.

$J_{i,j}$  is homogeneous between NV pairs. We choose the lattice constant to ensure that the average interaction strength matches that of the randomly distributed NV centers. Remarkably, even for systems on the lattice with comparable interaction strengths and imperfections, we observe qualitatively distinct behaviors.

As shown in Fig. 12(a), with small rotation imperfection, the simulated spin polarization of randomly distributed NV center (blue) exhibits robust subharmonic oscillations. In contrast, spins arranged on a regular lattice (red) display a fast decay in oscillation amplitudes. We further analyze the dynamics in the frequency domain, by performing Fourier transform over three time windows. Focusing on the  $(N_1, 0)$  response, the randomly distributed NV centers exhibit a slow decay in amplitude, highlighting the critical thermalization enabled by the disorder in the interaction term. In comparison, the oscillation amplitude on a regular lattice shows a fast decay.

On the other hand, when the rotation imperfections are large [Fig. 12(b)], the subharmonic response of NV centers positioned on a lattice splits into two distinct peaks, whereas randomly distributed NV centers maintain a robust DTQC response. These results underline the pivotal role of positional randomness slowing down thermalization dynamics and, thus, stabilizing the DTQC.

- 
- [1] P. M. Chaikin, T. C. Lubensky, and T. A. Witten, *Principles of Condensed Matter Physics* (Cambridge University Press, Cambridge, England, 1995), Vol. 10.
  - [2] S. Sachdev, *Quantum phase transitions*, *Phys. World* **12**, 33 (1999).
  - [3] F. Wilczek, *Quantum time crystals*, *Phys. Rev. Lett.* **109**, 160401 (2012).
  - [4] F. Wilczek, *Superfluidity and space-time translation symmetry breaking*, *Phys. Rev. Lett.* **111**, 250402 (2013).
  - [5] D. V. Else, C. Monroe, C. Nayak, and N. Y. Yao, *Discrete time crystals*, *Annu. Rev. Condens. Matter Phys.* **11**, 467 (2020).
  - [6] V. Khemani, A. Lazarides, R. Moessner, and S. L. Sondhi, *Phase structure of driven quantum systems*, *Phys. Rev. Lett.* **116**, 250401 (2016).
  - [7] C. W. von Keyserlingk and S. L. Sondhi, *Phase structure of one-dimensional interacting Floquet systems. II. Symmetry-broken phases*, *Phys. Rev. B* **93**, 245146 (2016).
  - [8] D. V. Else, B. Bauer, and C. Nayak, *Floquet time crystals*, *Phys. Rev. Lett.* **117**, 090402 (2016).
  - [9] D. V. Else, B. Bauer, and C. Nayak, *Prethermal phases of matter protected by time-translation symmetry*, *Phys. Rev. X* **7**, 011026 (2017).
  - [10] W. W. Ho, S. Choi, M. D. Lukin, and D. A. Abanin, *Critical time crystals in dipolar systems*, *Phys. Rev. Lett.* **119**, 010602 (2017).
  - [11] R. Moessner and S. L. Sondhi, *Equilibration and order in quantum Floquet matter*, *Nat. Phys.* **13**, 424 (2017).
  - [12] F. Harper, R. Roy, M. S. Rudner, and S. Sondhi, *Topology and broken symmetry in Floquet systems*, *Annu. Rev. Condens. Matter Phys.* **11**, 345 (2020).
  - [13] N. Y. Yao, A. C. Potter, I.-D. Potirniche, and A. Vishwanath, *Discrete time crystals: Rigidity, criticality, and realizations*, *Phys. Rev. Lett.* **118**, 030401 (2017).
  - [14] N. Y. Yao, C. Nayak, L. Balents, and M. P. Zaletel, *Classical discrete time crystals*, *Nat. Phys.* **16**, 438 (2020).
  - [15] X. Mi *et al.*, *Time-crystalline eigenstate order on a quantum processor*, *Nature (London)* **601**, 531 (2022).
  - [16] A. Lazarides and R. Moessner, *Fate of a discrete time crystal in an open system*, *Phys. Rev. B* **95**, 195135 (2017).
  - [17] P. Frey and S. Rachel, *Realization of a discrete time crystal on 57 qubits of a quantum computer*, *Sci. Adv.* **8**, eabm7652 (2022).
  - [18] J. Rovny, R. L. Blum, and S. E. Barrett, *Observation of discrete-time-crystal signatures in an ordered dipolar many-body system*, *Phys. Rev. Lett.* **120**, 180603 (2018).
  - [19] X. Yang and Z. Cai, *Dynamical transitions and critical behavior between discrete time crystal phases*, *Phys. Rev. Lett.* **126**, 020602 (2021).
  - [20] H. Keßler, J. G. Cosme, C. Georges, L. Mathey, and A. Hemmerich, *From a continuous to a discrete time crystal in a dissipative atom-cavity system*, *New J. Phys.* **22**, 085002 (2020).
  - [21] H. Taheri, A. B. Matsko, L. Maleki, and K. Sacha, *All-optical dissipative discrete time crystals*, *Nat. Commun.* **13**, 848 (2022).
  - [22] A. Kuroś *et al.*, *Phase diagram and optimal control for n-tupling discrete time crystal*, *New J. Phys.* **22**, 095001 (2020).
  - [23] W. C. Yu, J. Tangpanitanon, A. W. Glaetzle, D. Jaksch, and D. G. Angelakis, *Discrete time crystal in globally driven interacting quantum systems without disorder*, *Phys. Rev. A* **99**, 033618 (2019).
  - [24] F. M. Gambetta, F. Carollo, A. Lazarides, I. Lesanovsky, and J. P. Garrahan, *Classical stochastic discrete time crystals*, *Phys. Rev. E* **100**, 060105(R) (2019).
  - [25] M. Ippoliti, K. Kechedzhi, R. Moessner, S. L. Sondhi, and V. Khemani, *Many-body physics in the NISQ era: Quantum programming a discrete time crystal*, *PRX Quantum* **2**, 030346 (2021).
  - [26] F. M. Gambetta, F. Carollo, M. Marcuzzi, J. P. Garrahan, and I. Lesanovsky, *Discrete time crystals in the absence of manifest symmetries or disorder in open quantum systems*, *Phys. Rev. Lett.* **122**, 015701 (2019).
  - [27] S. Liu, S.-X. Zhang, C.-Y. Hsieh, S. Zhang, and H. Yao, *Discrete time crystal enabled by Stark many-body localization*, *Phys. Rev. Lett.* **130**, 120403 (2023).
  - [28] B. Ye, F. Machado, and N. Y. Yao, *Floquet phases of matter via classical prethermalization*, *Phys. Rev. Lett.* **127**, 140603 (2021).
  - [29] P. Kongkhambut *et al.*, *Observation of a continuous time crystal*, *Science* **377**, 670 (2022).
  - [30] S. Autti, V. B. Eltsov, and G. E. Volovik, *Observation of a time quasicrystal and its transition to a superfluid time crystal*, *Phys. Rev. Lett.* **120**, 215301 (2018).



- [31] H. Keßler, P. Kongkhambut, C. Georges, L. Mathey, J. G. Cosme, and A. Hemmerich, *Observation of a dissipative time crystal*, *Phys. Rev. Lett.* **127**, 043602 (2021).
- [32] W. Beatriz et al., *Critical prethermal discrete time crystal created by two-frequency driving*, *Nat. Phys.* **19**, 407 (2023).
- [33] M. P. Zaletel, M. Lukin, C. Monroe, C. Nayak, F. Wilczek, and N. Y. Yao, *Colloquium: Quantum and classical discrete time crystals*, *Rev. Mod. Phys.* **95**, 031001 (2023).
- [34] L. Xiang et al., *Long-lived topological time-crystalline order on a quantum processor*, *Nat. Commun.* **15**, 8963 (2024).
- [35] B. Huang, Y.-H. Wu, and W. V. Liu, *Clean Floquet time crystals: Models and realizations in cold atoms*, *Phys. Rev. Lett.* **120**, 110603 (2018).
- [36] T. Chen, R. Shen, C. H. Lee, B. Yang, and R. W. Bomantara, *A robust large-period discrete time crystal and its signature in a digital quantum computer*, [arXiv:2309.11560](https://arxiv.org/abs/2309.11560).
- [37] P. T. Dumitrescu, R. Vasseur, and A. C. Potter, *Logarithmically slow relaxation in quasiperiodically driven random spin chains*, *Phys. Rev. Lett.* **120**, 070602 (2018).
- [38] S. Sarkar and Y. Dubi, *Emergence and dynamical stability of a charge time-crystal in a current-carrying quantum dot simulator*, *Nano Lett.* **22**, 4445 (2022).
- [39] D. Vu and S. D. Sarma, *Dissipative prethermal discrete time crystal*, *Phys. Rev. Lett.* **130**, 130401 (2023).
- [40] A. Stasiuk and P. Cappellaro, *Observation of a prethermal  $U(1)$  discrete time crystal*, *Phys. Rev. X* **13**, 041016 (2023).
- [41] M. Lei et al., *Quantum thermalization and Floquet engineering in a spin ensemble with a clock transition*, [arXiv:2408.00252](https://arxiv.org/abs/2408.00252).
- [42] L. J. I. Moon et al., *Experimental observation of a time rondeau crystal: Temporal disorder in spatiotemporal order*, [arXiv:2404.05620](https://arxiv.org/abs/2404.05620).
- [43] S. Choi et al., *Observation of discrete time-crystalline order in a disordered dipolar many-body system*, *Nature (London)* **543**, 221 (2017).
- [44] J. Zhang et al., *Observation of a discrete time crystal*, *Nature (London)* **543**, 217 (2017).
- [45] D. V. Else, W. W. Ho, and P. T. Dumitrescu, *Long-lived interacting phases of matter protected by multiple time-translation symmetries in quasiperiodically driven systems*, *Phys. Rev. X* **10**, 021032 (2020).
- [46] H. Zhao, F. Mintert, and J. Knolle, *Floquet time spirals and stable discrete-time quasicrystals in quasiperiodically driven quantum many-body systems*, *Phys. Rev. B* **100**, 134302 (2019).
- [47] P. Bruno, *Comment on “Quantum time crystals”: A new paradigm or just another proposal of perpetuum mobile?*, *Phys. Rev. Lett.* **110**, 118901 (2013).
- [48] P. Bruno, *Impossibility of spontaneously rotating time crystals: A no-go theorem*, *Phys. Rev. Lett.* **111**, 070402 (2013).
- [49] H. Watanabe and M. Oshikawa, *Absence of quantum time crystals*, *Phys. Rev. Lett.* **114**, 251603 (2015).
- [50] K. Sacha, *Modeling spontaneous breaking of time-translation symmetry*, *Phys. Rev. A* **91**, 033617 (2015).
- [51] A. Pizzi, J. Knolle, and A. Nunnenkamp, *Period- $n$  discrete time crystals and quasicrystals with ultracold bosons*, *Phys. Rev. Lett.* **123**, 150601 (2019).
- [52] G. Kucsko et al., *Critical thermalization of a disordered dipolar spin system in diamond*, *Phys. Rev. Lett.* **121**, 023601 (2018).
- [53] The angular dependence of the dipolar interaction,  $J_{i,j}$ , can be both positive and negative. For a polarized initial state, the effective temperature of the resulting prethermal state is nearly infinite, rendering it featureless and incapable of supporting order [39,54].
- [54] G. He, B. Ye, R. Gong, Z. Liu, K. W. Murch, N. Y. Yao, and C. Zu, *Quasi-Floquet prethermalization in a disordered dipolar spin ensemble in diamond*, *Phys. Rev. Lett.* **131**, 130401 (2023).
- [55] Although neither the Hamiltonian nor the dynamics exhibits an exact periodicity, the power spectrum in the Fourier space can be thought of as a projection from the higher-dimensional Fourier spectrum. From this perspective, the dynamics of an observable is effectively a subharmonic response to the higher-dimensional Fourier spectrum of the drive.
- [56] D. M. Basko, I. L. Aleiner, and B. L. Altshuler, *Metal-insulator transition in a weakly interacting many-electron system with localized single-particle states*, *Ann. Phys. (Amsterdam)* **321**, 1126 (2006).
- [57] R. Nandkishore and D. A. Huse, *Many-body localization and thermalization in quantum statistical mechanics*, *Annu. Rev. Condens. Matter Phys.* **6**, 15 (2015).
- [58] D. A. Abanin, W. De Roeck, and F. Huveneers, *Exponentially slow heating in periodically driven many-body systems*, *Phys. Rev. Lett.* **115**, 256803 (2015).
- [59] M. Schreiber et al., *Observation of many-body localization of interacting fermions in a quasirandom optical lattice*, *Science* **349**, 842 (2015).
- [60] J. Smith et al., *Many-body localization in a quantum simulator with programmable random disorder*, *Nat. Phys.* **12**, 907 (2016).
- [61] J. Randall et al., *Many-body-localized discrete time crystal with a programmable spin-based quantum simulator*, *Science* **374**, 1474 (2021).
- [62] P. Peng, C. Yin, X. Huang, C. Ramanathan, and P. Cappellaro, *Floquet prethermalization in dipolar spin chains*, *Nat. Phys.* **17**, 444 (2021).
- [63] A. Kyprianidis et al., *Observation of a prethermal discrete time crystal*, *Science* **372**, 1192 (2021).
- [64] M. Gallone and B. Langella, *Prethermalization and conservation laws in quasi-periodically driven quantum systems*, *J. Stat. Phys.* **191**, 100 (2024).
- [65] E. J. Davis et al., *Probing many-body dynamics in a two-dimensional dipolar spin ensemble*, *Nat. Phys.* **19**, 836 (2023).
- [66] R. Gong et al., *Coherent dynamics of strongly interacting electronic spin defects in hexagonal boron nitride*, *Nat. Commun.* **14**, 3299 (2023).
- [67] R. Gong et al., *Isotope engineering for spin defects in van der Waals materials*, *Nat. Commun.* **15**, 104 (2024).
- [68] G. He, B. Ye, R. Gong, C. Yao, Z. Liu, K. Murch, N. Yao, and C. Zu, *Raw data: Experimental realization of discrete time quasi-crystals*, Zenodo (2024), <https://zenodo.org/records/14791637>.
- [69] V. Jacques et al., *Dynamic polarization of single nuclear spins by optical pumping of nitrogen-vacancy color centers*



- in diamond at room temperature*, [Phys. Rev. Lett. \*\*102\*\*, 057403 \(2009\)](#).
- [70] R. Fischer, A. Jarmola, P. Kehayias, and D. Budker, *Optical polarization of nuclear ensembles in diamond*, [Phys. Rev. B \*\*87\*\*, 125207 \(2013\)](#).
- [71] C. Zu *et al.*, *Experimental realization of universal geometric quantum gates with solid-state spins*, [Nature \(London\) \*\*514\*\*, 72 \(2014\)](#).
- [72] G. D. Kahanamoku-Meyer and J. Wei, dynamite v0.3.1, 2023, [10.5281/zenodo.7706785](#).